Unmixing dynamic PET images for voxel-based kinetic component analysis

Yanna Cruz Cavalcanti, *Student Member, IEEE*, Thomas Oberlin, *Member, IEEE*,
Nicolas Dobigeon, *Senior Member, IEEE*, Simon Stute, Maria Ribeiro, Clovis Tauber, *Member, IEEE*

***Abstract*—To analyze dynamic positron emission tomography (PET) images, various generic multivariate data analysis techniques have been considered in the literature, such as clustering, principal component analysis (PCA), independent component analysis (ICA) and non-negative matrix factorization (NMF). Nevertheless, these conventional approaches generally fail to recover a reliable, understandable and interpretable description of the data. In this paper, we propose an alternative analysis paradigm based on the concept of linear unmixing as an efficient and meaningful way to analyze dynamic PET images. The time-activity curves (TACs) measured in the voxels are modeled as linear combinations of elementary component signatures weighted by their respective concentrations in each voxel. Additionally to the non-negativity constraint of NMF, the proposed unmixing approach ensures an exhaustive description of the mixtures by a sum-to-one constraint of the mixing coefficients. Besides, it allows both the noise and partial volume effects to be handled. Moreover, the proposed method accounts for any possible fluctuations in the exchange rate of the tracer between the free compartment and a specifically bound ligand compartment. Indeed, it explicitly models the spatial variability of the corresponding signature through a perturbed specific binding component. The performance of the method is assessed on both synthetic and real data and compared to other conventional analysis methods.**

***Index Terms*—Dynamic PET image, deconvolution, unmixing, brain imaging.**

I. Introduction

DYNAMIC positron emission tomography (PET) is a non-invasive nuclear imaging technique that allows biological processes to be quantified and organ metabolic function to be evaluated through the three-dimensional measure of the injected radiotracer concentration over time. This technique enables the distinction of specific regions from metabolism particularities not easily detected in other biomedical image modalities. It is of great interest in the diagnosis of numerous pathologies, ranging from Parkinson to Alzheimer diseases. Additionally, dynamic PET has also been increasingly used on the follow-up of treatment or disease evolution.

Part of this work is supported by CAPES.

Y. C. Cavalcanti, T. Oberlin and N. Dobigeon are with University of Toulouse, IRIT/INP-ENSEEIHT, CNRS, 2 rue Charles Camichel, BP 7122, 31071 Toulouse Cedex 7, France (e-mail: {Yanna.Cavalcanti, Thomas.Oberlin, Nicolas.Dobigeon,}@enseeiht.fr).

S. Stute is with UMRS Inserm U1023 IMIV-CEA SHFJ, 91400 Orsay, France (e-mail: simon.stute@cea.fr).

M. Ribeiro and C. Tauber are with UMRS Inserm U930 - Universit de Tours, 37032 Tours, France (e-mail: {maria.ribeiro,clovis.tauber}@univ-tours.fr).

The analysis of dynamic PET images, in particular the quantification of the kinetic properties of the tracer, yet remains a difficult and challenging issue. Therefore, various methods have been proposed in the context of post-reconstruction dynamic PET image analysis to either reduce the noise, correct for partial volume effect or better facilitate image segmentation by clustering voxels with similar kinetics into groups.

Many unsupervised approaches have been proposed based on the hypothesis that voxels belonging to the same region can be identified from the similarity between their TACs. Thus, segmentation has constantly appeared as a relevant tool in the analysis of dynamic PET, often implemented as clustering of time-activity-curves (TACs). Clustering the sinogram domain by maximizing the posterior probability was proposed by Kamasak [1]. An algorithm similar to K-means proposed by Wong et al. [2] improves the standard method with a least-square distance minimizing a within-cluster cost. Ashburner et al. [3] applied a clustering approach based on the shapes of the voxel TACs rather than their absolute value while Brankov et al. [4] used a similarity metric. A parametric imaging algorithm based on an average linkage method for hierarchical cluster was presented by Zhou et al. [5] while Guo et al. [6] combined hierarchical linkage with a precluster in a two-stage process. Maroy et al. [7] proposed a method of local mean analysis also based on hierarchical linkage. Liao and Qi [8] developed a weighted multiphase level set method to achieve segmentation. More recently, a spectral clustering method was proposed to map the data into a high dimensional space and then project and cluster it into a low-dimensional space [9]. While these methods can be effective in some situations, they all assume that a unique single kinetic process occurs in a given voxel, which is often far from the actual underlying physical mechanism. Indeed, several factors limit the validity of this assumption, such as the limited spatial resolution, partial volume effects and, more generally, biological heterogeneity [10].

To overcome this limitation, dynamic PET image analysis has been addressed within a blind source separation (BSS) framework where the TACs in each voxel are modeled as mixtures of elementary TACs. For instance, factor analysis of dynamic structures was proposed by Wu et al. [11]. In cardiac dynamic PET, independent component analysis (ICA) has been often used to distinguish between TACs from myocardium and ventricles (left and right) [12], [13]. ICA was also adopted by Chen et al. [14] to identify the carotid artery and surrounding tissues in a cubic region manually defined.

However, ICA assumes statistical independency of the sources to be recovered, which compromises its performance since TAC sources are expected to be correlated, short-numbered and with a very low signal-to-noise ratio (SNR) [15]. Conversely, deterministic approaches with weaker assumptions on the signal distributions were proposed. Physiological characteristics of images reconstructed with ordered subset expectation maximization (OSEM) are taken into account in NMF methods, popularized in the PET framework by Lee et al. [16]. Kim et al [17] applied NMF to the extraction of the carotid input function followed by a partial volume correction. A scale-corrected NMF was used in [18] for TAC estimation. Schulz et al. [19] used NMF to distinguish between myocardial tracer concentration and blood input function. Another deterministic approach applied to perform BSS on the non-negative data domain is the geometrical method implemented in the recent work of Ouedraogo et al. [20] based on the simplicial cone shrinking concept. While these approaches have proved some effectiveness for dynamic PET image analysis, they are hampered by several limitations. Among the principal challenges, these approaches face the non-uniqueness and the underdetermined nature of the optimization problem [21], which often leads to converging to a local minima. Moreover, they are sensitive to the initialization step because of the specific nature of dynamic PET image data.

Besides, dynamic PET provides a series of frames with varying durations that can reach from 10 seconds to 20 minutes. As an outcome of its short intervals of dynamic acquisition compared to static measurements, dynamic PET data is highly corrupted by noise, especially on the earlier frames that are kept short to capture the fast kinetics right after tracer injection. In order to recover spatial resolution and reduce noise, several works were led to spatially filter individual frames [22], [23]. However, these methods neglect the signal temporal consistency, benefiting only from single-frame information. This reasoning has recently led to an increasing interest on approaches acknowledging the time-course of the signal [24]–[27].

Moreover, TACs cannot be assumed to be driven by constant kinetic parameters over time. Indeed, they may suffer from fluctuations in the exchange rate of tracer between the free compartment and a specifically bound ligand compartment in the region of interest, which induces inaccuracies on compartment modeling [28] [10]. For instance, the findings of Schiepers et al. [29] show that the variations on the parameter representing the exchange of tracer between the free and a specifically bound ligand compartments could help differentiating lesions that were tumor predominant and treatment change predominant. The work of Kamasak [30] discussed the variations in compartment model parameters in connection with noise level in the TACs. He found errors around 26% in the parameter related to the specific binding region (SBR). Additionally, the reconstruction method applied to obtain the final PET image may induce changes on the noise distribution, especially concerning non-linear iterative techniques, such as OSEM, that often produce an object-dependent noise that is higher in regions with high uptake compared to low uptake regions [31], [32].

To address all these limitations and take into account the intrinsic properties of PET imaging, this paper proposes a new approach based on the *unmixing* concept to tackle the problem of dynamic PET image analysis. Also referred to as *spectral mixture analysis*, unmixing originates from the geoscience and remote sensing literature [33] and has proven its interest for other applicative context, such as microscopy [34] and genetics [35]. In this work, a parallel is drawn between hyperspectral images and dynamic PET images, where the TACs of the PET image are the counterparts of the spectra. Thus, with an original variational formulation, each PET voxel TAC is decomposed as a weighted combination of pure physiological factors, referred to as endmembers. Moreover, compared to other approaches proposed in the PET image analysis literature, the proposed mixing-based model has the great advantage of explicitly accounting for spatial dependency between elementary TACs (i.e., endmembers) as well as other physical properties such as partial volume effects or spatial consistency. This both reduces the range of the possible solutions and increases the robustness and accuracy of the method compared to ICA and NMF counterparts, as the non-negativity constraint alone is not sufficient to assure the uniqueness of the factorization [36], [37]. Moreover, contrary to any concurrent methods of the literature, the proposed model explicitly accounts for any spatial variability of the TAC corresponding to specific binding. This variability is voxel-wise decomposed onto a predefined dictionary whose atoms have been learned beforehand by conducting a principal component analysis on a learning dataset. The number of endmembers to be recovered is assumed to be a priori known, since the present work focuses on the analysis of images of brain where voxels only consist of volumes composed of tissue and blood. Additionally, the tissues are assumed to be of three types: non-specific gray matter, white matter and specific gray matter. Each voxel TAC is therefore supposed to be a combination of these 4 endmember TACs.

The sequel of this paper is organized as follows. The proposed mixing-based analysis model is described in Section II. Section III presents the corresponding unmixing algorithm able to recover the endmembers, their corresponding proportions in each voxel and the variability maps. Simulation results obtained with synthetic data are reported in Section IV. Experimental results on real data are provided in Section V. Section VI concludes the paper.

II. Problem Statement

A. Perturbed specific binding endmember linear mixing model (PSBE-LMM)

Consider N voxels of a 3D dynamic PET image acquired in L successive time-frames. First, we omit the partial volume effects, i.e., the spatial blurring induced by the point spread function (PSF) of the instrument, and any measurement noise. The TAC in the n^{th} voxel ($n \in \{1, \ldots, N\}$) over the L time-frames is denoted $\mathbf{x}_n = [x_{1,n}, \ldots, x_{L,n}]^T$. Inspired by the linear mixing model (LMM) popularized in the remote sensing literature [33], each TAC $\mathbf{x}_n$ is assumed to be a linear

combination of K elementary signatures $\mathbf{m}_k$, referred to as *endmembers*,

$$\mathbf{x}_n = \sum_{k=1}^{K} \mathbf{m}_k a_{k,n}, \tag{1}$$

where $\mathbf{m}_k = [m_{1,k}, \ldots, m_{L,k}]^T$ denotes the TAC of a pure voxel of the k^{th} tissue type and $a_{k,n}$ is the fraction (referred to as *abundances*) of the k^{th} tissue in the n^{th} observation. The endmember signatures $\mathbf{m}_k$ $(k = 1, \ldots, K)$ can for instance correspond to the kinetics of the radiotracer in a particular tissue, the blood, the gray or white matters.

In the present study, contrary to conventional factor analysis techniques (e.g., PCA, ICA and NMF), one wants to explicitly account for any fluctuation of the kinetic parameters driving the TAC associated with the SBR, denoted $\mathbf{m}_1$ without loss of generality. As a consequence, this so-called specific binding endmember (SBE) is assumed to be subjected to spatial variability. Endmember variability is a concept that has received increased interest in the hyperspectral domain in recent years as it allows changes on lightening and environment to be taken into account [38], [39]. Recently, Thouvenin et al. have proposed a perturbed LMM (PLMM) to further address this problem [40]. In this work, PLMM is specifically adapted to the dynamic PET image framework, where variability is expected to mainly affect the SBE TAC $\mathbf{m}_1$ while the possible fluctuations in the TACs $\mathbf{m}_k$ $(k \in \{2, \ldots, K\})$ related to free or non-specific bound compartments are neglected. Thus, to properly model this spatial variability, the SBE TAC will be now spatially indexed. Moreover, according to the PLMM, the SBE TAC in a given voxel is modeled as a spatially-variant additive perturbation affecting a nominal/common SBE signature $\bar{\mathbf{m}}_1$

$$\mathbf{m}_{1,n} = \bar{\mathbf{m}}_1 + \delta\mathbf{m}_{1,n}, \tag{2}$$

where the additive term $\delta\mathbf{m}_{1,n}$ describes its spatial variability over the image. Having in mind the subsequent resulting estimation problem, recovering the spatial fluctuation $\delta\mathbf{m}_{1,n}$ in each image voxel may be a challenging issue. Fortunately, benefiting from generative models or available datasets for most SBE signatures, the possible TACs $\mathbf{m}_{1,n}$ are expected to be described by a small number N_v of degrees of freedom with $N_v \ll L$. As a consequence, similarly to the strategy followed in [41], the additive terms $\delta\mathbf{m}_{1,n}$ $(n \in \{1, \ldots, N\})$ are assumed to be approximated by the linear expansion

$$\delta\mathbf{m}_{1,n} = \sum_{i=1}^{N_v} b_{i,n}\mathbf{v}_i, \tag{3}$$

where the N_v variability basis elements and the nominal SBR signature $\bar{\mathbf{m}}_1$ can be chosen beforehand, e.g., by conducting a PCA on a learning set composed of simulated or measured SBE TACs. Thus, the set of coefficients $\{b_{1,n}, \ldots, b_{N_v,n}\}$ quantify the amount of variability in the n^{th} voxel.

Combining the linear mixing model (1), the perturbation model (2) and its linear expansion (3), the voxel TACs are described according to the following so-called perturbed SBE linear mixing model (PSBE-LMM)

$$\mathbf{x}_n = a_{1,n}\left(\bar{\mathbf{m}}_1 + \sum_{i=1}^{N_v} b_{i,n}\mathbf{v}_i\right) + \sum_{k=2}^{K} a_{k,n}\mathbf{m}_k. \tag{4}$$

To be fully comprehensive, this work also proposes to explicitly model the PET scan PSF, combining a deconvolution step jointly with parameter estimation. We will denote by $\mathbf{H}$ the linear operator that computes the 3D convolution by some known PSF.

$$\mathbf{Y} = \mathbf{MAH} + \underbrace{\left[\mathbf{E}_1\mathbf{A} \circ \mathbf{VB}\right]\mathbf{H}}_{\Delta} + \mathbf{R}, \tag{5}$$

where $\mathbf{M} = [\bar{\mathbf{m}}_1, ..., \mathbf{m}_k]$ is a $L \times K$ matrix containing the endmember TACs, $\mathbf{A} = [\mathbf{a}_1, \ldots, \mathbf{a}_n]$ is a $K \times N$ matrix composed of the abundance vectors $\mathbf{a}_n = [a_{1,n}, \ldots, a_{K,n}]^T$, "$\circ$" is the Hadamard point-wise product, $\mathbf{E}_1$ is the matrix $[\mathbf{1}_{L,1}\mathbf{0}_{L,K-1}]$, $\mathbf{V} = [\mathbf{v}_1, \ldots, \mathbf{v}_{N_v}]$ is the $L \times N_v$ matrix containing the basis elements used to expand the spatially variability of the SBE TAC, $\mathbf{B} = [\mathbf{b}_1, \ldots, \mathbf{b}_n]$ is the $N_v \times N$ matrix containing the intrinsic abundances $\mathbf{b}_n = [b_{1,n}, \ldots, b_{N_v,n}]^T$, and $\mathbf{R} = [\mathbf{r}_1, \ldots, \mathbf{r}_N]^T$ is an $L \times N$ matrix accounting for noise and mismodeling. The voxel-wise terms $\mathbf{r}_n = [r_{1,n}, \ldots, r_{L,n}]$ $(n \in \{1, \ldots, N\})$ are additive zero-mean Gaussian sequences assumed to be independent and identically distributed (i.i.d.) to fit the signal encountered in PET often recognized to follow a Poisson or Gaussian distribution even when the radioactivity concentration is heterogeneous [8], [42], [43].

Besides, additional constraints regarding these set of parameters are assumed. First, non-negativity and sum-to-one constraints are usually considered to reflect physical considerations related to the abundances

$$\begin{aligned} \mathbf{A} &\succeq \mathbf{0}_{K,N}, \\ \mathbf{A}^T\mathbf{1}_k &= \mathbf{1}_N, \end{aligned} \tag{6}$$

where $\succeq$ stands for a component-wise inequality, that is, $a_{k,n} \in [0, 1]$ and the sum of the abundances of all elementary TACs must be 1 for each voxel. Since the PET images are reconstructed by OSEM approaches, they are known to be non-negative and, consequently, its endmembers are also defined as greater or equal to 0

$$\mathbf{M} \succeq \mathbf{0}_{L,K}. \tag{7}$$

To avoid spurious ambiguity, we also consider the following assumption on the intrinsic variability proportion matrix of the observed images

$$\mathbf{B} \succeq \mathbf{0}_{N_v,N}. \tag{8}$$

We accordingly fix the nominal SBE TAC $\bar{\mathbf{m}}_1$ with a robust estimation of the TAC chosen as a lower bounding of a set of previously generated or measured SBE TACs. This means that a negative bias on the SBE TAC is introduced to model the spatially-varying SBE TACs $\mathbf{m}_{1,n}$ $(n \in \{1, \ldots, N\})$ and alternatively compensated by a variability that is distorted by the same quantity but positively. This constraint is chosen to avoid a high correlation between the other endmember TACs

and $\sum_{i=1}^{N_v} \mathbf{v}_i b_{i,n}$ when $b_{i,n}$ is allowed to be negative. Based on this model, the unmixing-based analysis of dynamic PET images is formulated in the next paragraph.

B. Problem formulation

The PSBE-LMM (5) and constraints (6) and (7) can be combined to formulate a constrained optimization problem. In order to estimate the matrices $\mathbf{M}$, $\mathbf{A}$, $\mathbf{B}$, a proper cost function is defined. As mentioned above, it is suitable to assume PET image noise to follow a Gaussian distribution. Therefore the data-fitting term is defined through the Frobenious norm $\|\cdot\|_F^2$ of the difference between the dynamic PET image $\mathbf{Y}$ and proposed data modeling $\mathbf{MAH} + \Delta$. Since the problem is ill-posed and non-convex, additional regularizers become essential. In this paper, we propose to define penalization functions Φ, Ψ and Ω to reflect the available *a priori* knowledge on $\mathbf{M}$, $\mathbf{A}$ and $\mathbf{B}$, respectively. The optimization problem is then defined as

$$(\mathbf{M}^*, \mathbf{A}^*, \mathbf{B}^*) \in \underset{\mathbf{M},\mathbf{A},\mathbf{B}}{\arg\min} \Big\{ \mathcal{J}(\mathbf{M}, \mathbf{A}, \mathbf{B}) \text{ s.t. } (6)\text{–}(8) \Big\}, \quad (9)$$

with

$$\mathcal{J}(\mathbf{M}, \mathbf{A}, \mathbf{B}) = \frac{1}{2} \Big\| \mathbf{Y} - \mathbf{MAH} - \Big[\mathbf{E}_1 \mathbf{A} \circ \mathbf{VB}) \Big] \mathbf{H} \Big\|_F^2 + \alpha \Phi(\mathbf{A}) + \beta \Psi(\mathbf{M}) + \lambda \Omega(\mathbf{B}), \quad (10)$$

where the parameters α, β and λ control the trade-off between the data fitting term and the penalties $\Phi(\mathbf{A})$, $\Psi(\mathbf{M})$ and $\Omega(\mathbf{B})$, described hereafter.

1) Abundance penalization: TACs from neighboring voxels often present similar behavior as they may belong to the same tissue or organ. To incorporate this characteristics, the following spatial smoothness penalization is applied to the abundances.

$$\Phi(\mathbf{A}) = \frac{1}{2} \|\mathbf{AS}\|_F^2, \quad (11)$$

where $\mathbf{S}$ is a matrix $N \times 3N$computing the first-order spatial finite differences, i.e., the differences between neighboring voxels. In our case, the considered PET image is of three dimensions, leading to the neighborhood system depicted in Fig. (1).

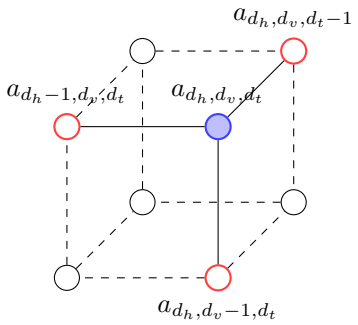

Fig. 1. Diagram of voxel neighborhood structure for three dimensions, where the blue voxel is the one considered and the red ones are its direct neighbors.

The first order finite differences in the three directions x,y and z are then defined for each pixel as

$$[\mathbf{AS}]_{x,y,z} = \begin{bmatrix} a_{x,y,z} - a_{x-1,y,z} \\ a_{x,y,z} - a_{x,y-1,z} \\ a_{z,x,z} - a_{x,y,z-1} \end{bmatrix}.$$

On the boundaries, finite differences are not taken into account. The transposed matrix $\mathbf{S}^T$, which will appear in gradient computation of the penalization, results also in a first-order finite difference calculus but in the other sense for each direction. Note also that the application of both $\mathbf{S}$ and $\mathbf{S}^T$ leads to a discrete 3D Laplacian.

2) Endmember penalization: The chosen endmember penalization benefits from the availability of rough endmember TACs estimates $\mathbf{M}^0 = [\tilde{\mathbf{m}}_1^0, \ldots, \mathbf{m}_K^0]$. Thus, we propose to enforce similarity (in term of mutual Euclidean distances) between these primary estimates and the endmember TACs to be recovered

$$\Psi(\mathbf{M}) = \frac{1}{2} \|\mathbf{M} - \mathbf{M}^0\|_F^2. \quad (12)$$

3) Variability penalization: The SBE TAC variability is expected to be spatially localized since only affecting a small number of voxels, in particular those belonging the SBR. As a consequence, we propose to enforce sparsity via the use of the ℓ_1-norm, also known as the LASSO regularizer [44]

$$\Omega(\mathbf{B}) = \|\mathbf{B}\|_1, \quad (13)$$

where $\|.\|_1$ is the ℓ_1 norm. This penalty forces $b_{i,n}$ to be 0 outside the SBR, thus reducing overfitting.

III. A PALM-based algorithm

Given the nature of the optimization problem (9) to be solved, which is genuinely nonconvex and nonsmooth, the minimization strategy is the proximal alternating linearized minimization (PALM) scheme [45]. PALM is an iterative, gradient-based algorithm which generalizes the Gauss-Seidel method. It consists in iterating with respect to $\mathbf{A}$, $\mathbf{M}$ and $\mathbf{B}$ and ensures convergence to a local critical point $\mathbf{A}^*$, $\mathbf{M}^*$ and $\mathbf{B}^*$. The principle of PALM is briefly recalled in the following section. Then it will be specifically instantiated for the unmixing-based kinetic component analysis considered in this paper.

A. PALM: general principle

PALM is based on alternating partial gradient steps coupled with a proximal mapping. For simplicity purposes, a nonconvex-nonsmooth problem composed of two block of variables $x \in \mathbb{R}^n$ and $y \in \mathbb{R}^m$

$$\min_{x,y} \Psi(x, y) := f(x) + g(y) + H(x, y)$$

is considered where $H(\cdot, \cdot)$ is a smooth and gradient-Lipschitz coupling function and the functions f and g are extended valued (i.e., allow constraints to be included). PALM consists in alternating the proximal forward backward steps, as summarized in Algo. 1.

Algorithm 1: PALM: Proximal Alternating Linearized Minimization

Initialization: $\left(x^0, y^0\right) \in \mathbb{R}^n \times \mathbb{R}^m$
Input: Algorithmic parameters $\gamma_1 > 1$ and $\gamma_2 > 1$
$k \leftarrow 0$
for $k \geq 1$ **do**
  Set $c_k = \frac{L_x(y^k)}{\gamma}$
  Compute $x^{k+1} \in \text{prox}_{\frac{f}{c_k}}\left(x^k - \frac{1}{c_k}\nabla_x H(x^k, y^k)\right)$
  Set $d_k = \frac{L_y(x^{k+1})}{\gamma}$
  Compute $y^{k+1} \in \text{prox}_{\frac{g}{d_k}}\left(y^k - \frac{1}{d_k}\nabla_y H(x^{k+1}, y^k)\right)$
  $k \leftarrow k + 1$
Result: A sequence $\left\{\left(x^k, y^k\right)\right\}_{k\geq 0}$

Within this algorithmic scheme, prox_f denotes the proximal map associated to the function f defined as

$$\text{prox}_f(v) = \arg\min_x \left(f(x) + \frac{1}{2}\|x - v\|_2^2\right),$$

γ is a constant ensuring the convergence of the algorithm and may be fixed at, e.g., 0,99, and $L_x(y)$ and $L_y(x)$ are the Lipschitz constants of the gradients $\nabla_x H(x, y)$ and $\nabla_y H(x, y)$, respectively, satisfying for all x_1, x_2:

$$\|\nabla_x H(x_1, y) - \nabla_x H(x_2, y)\| \leq L_x(y)\|x_1 - x_2\|,$$

and likewise for $\nabla_y H(x, y)$.

This general principle is applied to solve the unmixing problem. The resulting PSBE-LMM unmixing algorithm is sketched in Algo 2 whose main steps are described in the following paragraphs.

Algorithm 2: PSBE-LMM unmixing: global algorithm

Data: $\mathbf{Y}$
Input: $\mathbf{A}^0$, $\mathbf{M}^0$, $\mathbf{B}^0$
$k \leftarrow 0$
while *stopping criterion not satisfied* **do**
  $\mathbf{M}^{k+1} \leftarrow \mathcal{P}_+\left(\mathbf{M}^k - \frac{\gamma}{L_M^k}\nabla_{\mathbf{M}}\mathcal{J}(\mathbf{M}^k, \mathbf{A}^{k+1}, \mathbf{B}^k)\right)$
  $\mathbf{A}^{k+1} \leftarrow \mathcal{P}_{\mathcal{A}_R}\left(\mathbf{A}^k - \frac{\gamma}{L_A^k}\nabla_{\mathbf{A}}\mathcal{J}(\mathbf{M}^k, \mathbf{A}^k, \mathbf{B}^k)\right)$
  $\mathbf{B}^{k+1} \leftarrow \text{prox}_{\frac{\lambda}{L_B^k}\|.\|_1}\left(\mathcal{P}_+\left(\mathbf{B}^k - \frac{\gamma}{L_B^k}\nabla_{\mathbf{B}}\mathcal{J}(\mathbf{M}^{k+1}, \mathbf{A}^{k+1}, \mathbf{B}^k)\right)\right)$
  $k \leftarrow k + 1$
$\mathbf{A} \leftarrow \mathbf{A}^{k+1}$
$\mathbf{M} \leftarrow \mathbf{M}^{k+1}$
$\mathbf{B} \leftarrow \mathbf{B}^{k+1}$
Result: $\mathbf{A}$, $\mathbf{M}$, $\mathbf{B}$

B. Optimization with respect to $\mathbf{M}$

A direct application of [45] under the constraints defined by (7) leads to the following updating rule

$$\mathbf{M}^{k+1} = \mathcal{P}_+\left(\mathbf{M}^k - \frac{1}{L_M^k}\nabla_{\mathbf{M}}\mathcal{J}(\mathbf{M}^k, \mathbf{A}^{k+1}, \mathbf{B}^k)\right), \quad (14)$$

where $\mathcal{P}_+(\cdot)$ is the projector onto the nonnegative set $\{\mathbf{X}|\mathbf{X} \succeq \mathbf{0}_{L,R}\}$ and the required gradient is written[1]

$$\begin{aligned}\nabla_{\mathbf{M}}\mathcal{J}(\mathbf{M}, \mathbf{A}, \mathbf{B}) = &\left((\mathbf{E}_1\mathbf{A} \circ \mathbf{VB})\,\mathbf{H} - \mathbf{Y}\right)\mathbf{H}^T\mathbf{A}^T \\ &+\mathbf{M}(\mathbf{AHH}^T\mathbf{A}^T) + \beta(\mathbf{M} - \mathbf{M}^0),\end{aligned} \quad (15)$$

Moreover, L_M^k is a bound on the Lipschitz constant of $\nabla_{\mathbf{M}}\mathcal{J}(\mathbf{M}^k, \mathbf{A}^{k+1}, \mathbf{B}^k)$, defined as

$$L_M = \left\|\mathbf{AHH}^T\mathbf{A}^T\right\| + \beta. \quad (16)$$

It is important to note that this value may be not optimal and a lower value can be found to accelerate the updates.

C. Optimization with respect to $\mathbf{A}$

Similarly to paragraph III-B, the abundance update is defined as the following

$$\mathbf{A}^{k+1} = \mathcal{P}_{\mathcal{A}_R}\left(\mathbf{A}^k - \frac{1}{L_A^k}\nabla_{\mathbf{A}}\mathcal{J}(\mathbf{M}^k, \mathbf{A}^k, \mathbf{B}^k)\right), \quad (17)$$

where $\mathcal{P}_{\mathcal{A}_R}(\cdot)$ is the projection on the set $\mathcal{A}_R$ defined by the abundance constraints (6), which can be computed with efficient algorithms, see, e.g., [46]. The gradient can be computed as

$$\nabla_{\mathbf{A}}\mathcal{J}(\mathbf{M}, \mathbf{A}, \mathbf{B}) = -\mathbf{M}^T(\mathbf{D}_A) - \mathbf{E}_1^T(\mathbf{D}_A \circ \mathbf{VB}) + \alpha\mathbf{ASS}^T, \quad (18)$$

with $\mathbf{D}_A = (\mathbf{Y} - \mathbf{MAH} - (\mathbf{E}_1\mathbf{A} \circ \mathbf{VB})\mathbf{H})\mathbf{H}^T$. Moreover, L_A^k is the Lipschitz constant of $\nabla_{\mathbf{A}}\mathcal{J}(\mathbf{M}^k, \mathbf{A}^k, \mathbf{B}^k)$.

$$\begin{aligned}L_A = \|\mathbf{H}\|^2\Big(&\|\mathbf{E}_1\|\|\mathbf{VB}\|(2\|\mathbf{M}\|_\infty + \|\mathbf{E}_1\|\|\mathbf{VB}\|_\infty)\Big) \\ &+ \|\mathbf{H}\|^2\|\mathbf{M}^T\mathbf{M}\| + \alpha\|\mathbf{SS}^T\|,\end{aligned} \quad (19)$$

where the spectral norm $\|\mathbf{X}\| = \sigma_{\max}(\mathbf{X})$ is the largest singular value of $\mathbf{X}$ and $\|\mathbf{X}\|_\infty = \max_{1\leq i\leq m}\sum_{j=1}^n |x_{ij}|$ is the sum of the absolute values of the matrix row entries.

D. Optimization with respect to $\mathbf{B}$

Finally, the updating rule for the variability coefficients can be written as

$$\mathbf{B}^{k+1} = \text{prox}_{\frac{\lambda}{L_B^k}\|.\|_1}\left(\mathcal{P}_+\left(\mathbf{B}^k - \frac{1}{L_B^k}\nabla_{\mathbf{B}}\mathcal{J}(\mathbf{M}^{k+1}, \mathbf{A}^{k+1}, \mathbf{B}^k)\right)\right), \quad (20)$$

where the proximal mapping operator is the soft-thresholding operator

$$\left[\text{prox}_{c\|\cdot\|_1}(\mathbf{v})\right]_i = \begin{cases} v_i - c & v_i \geq c \\ 0 & |v_i| \leq c \\ v_i + c & v_i \leq -c \end{cases}. \quad (21)$$

[1]Note that the iteration index has been omitted in the following definitions of the Lipschitz constants to lighten the notations.

Indeed, the proximal map of the sum of the nonnegative indicator function and the ℓ_1 norm is exactly the composition of the proximal maps of both individual functions, following the same principle showed in [45]. The gradient writes

$$\nabla_{\mathbf{B}}\mathcal{J}(\mathbf{M},\mathbf{A},\mathbf{B}) = \mathbf{V}^T\left((\mathbf{E}_1\mathbf{A})\circ(-\mathbf{Y}+\mathbf{MAH}+\Delta)\,\mathbf{H}^T\right)$$

and L_B^k is the Lipschitz constant of $\nabla_{\mathbf{B}}\mathcal{J}(\mathbf{M}^{k+1},\mathbf{A}^{k+1},\mathbf{B}^k)$

$$L_B = \|\mathbf{E}_1\mathbf{A}\|_\infty^2\|\mathbf{V}\|^2\|\mathbf{H}\|^2. \tag{22}$$

IV. Evaluation on Synthetic Data

A. Synthetic data generation

To illustrate the accuracy of our algorithm, experiments are first conducted on synthetic data for which ground truth for the main parameters of interest (i.e., endmember TACs and abundance maps) is known. In the clinical PET framework, ground truth concerning the tracer kinetics and uptake is never completely known. Studies with physical phantoms can be a solution for having a ground truth. They are often used in the context of static PET acquisitions. However, when interested in tracer kinetics, dynamic scans are not fully possible since phantoms can never truly represent realistic physiological processes that occur in a real patient.

Meanwhile, simulations benefit from an entire knowledge of the patient properties and kinetics, and its degree of complexity and details can be selected according to the purpose of the study, e.g., by including or not different physical effects. Furthermore, several simulations can be performed in a reasonable time. In this context, simulations play an important role in the development of image processing approaches for dynamic PET studies.

Thus, simulations are conducted on a $128 \times 128 \times 64$ synthetic image. In this image, each voxel is constructed as a combination of $K = 4$ pure TACs representative of the brain, which is the organ of interest in the present work: specific gray matter, pure blood or veins, pure white matter and non-specific gray matter. First, a high resolution dynamic PET numerical phantom, showed in Fig. 2 with labeled regions of interest (ROIs) [47], has been used to create the ground truth for abundances and endmembers. In this phantom, all the distributions of the tracer per region have been extracted from a real dynamic PET acquisition and are observed in $L = 20$ times of acquisition ranging from 60 to 300s. To simulate realistic variability of the SBE TAC, a set of synthetic TACs generated through a realistic compartment-based model is used.

More precisely, the overall generation process is presented in Fig. 3 and described in what follows:

- The dynamic PET phantom showed in Fig. 2 has been first linearly unmixed using the N-FINDR [48] and SUnSAL [49] algorithms to select the ground-truth non-specific endmember TAC $\mathbf{m}_2, ..., \mathbf{m}_K$ and abundances $\mathbf{a}_1, \ldots, \mathbf{a}_N$, respectively. These endmember TACs and corresponding abundance maps are depicted in Fig. 6 (left) and Fig. 5 (left), respectively.
- From a compartment-based function, a large database has been created by randomly varying the k3 parameter (representing the specific binding rate of the radiotracer in the tissue). A PCA is conducted on this dataset, and an analysis of the eigenvalues leads to the choice of a unique variability basis element $\mathbf{V} = \mathbf{v}_1$ (i.e., $N_v = 1$), depicted in Fig. 4 (bottom).
- The nominal endmember TAC $\bar{\mathbf{m}}_1$ corresponding to the SBR is then chosen as the TAC of minimum area under the curve (AUC) among all the TACs of this database. This TAC is depicted in Fig. 4 (top, red curve).
- The 1st row of the abundance matrix $\mathbf{A}$, namely $\mathbf{A}_1 \triangleq [a_{1,1}, \ldots, a_{1,N}]$ was designed to locate the SBR. Then, the $N_v \times N$ matrix $\mathbf{B} = [b_1, \ldots, b_N]$ mapping the SBE TAC variability in each voxel has been randomly generated. The SBR is divided into 4 subregions with non-zero coefficients b_n, as shown in Fig. 7 (left),with 0 outside the SBR. In each of these subregions, these non-zeros coefficients have been drawn according to Gaussian distributions with a particular mean value and small variances. Some resulting spatially-varying SBE TACs in each region are showed in Fig. 4.

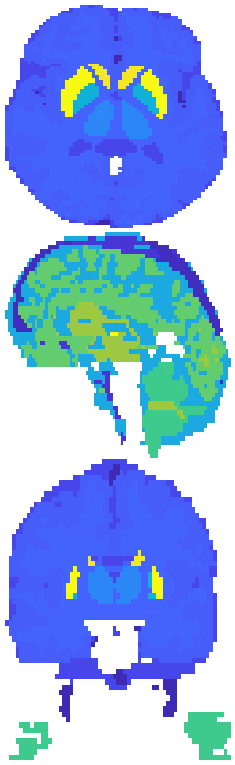

Fig. 2. 15th time-frame of dynamic PET phantom: from top to bottom, transversal, sagital and coronal planes

After this primary generation process, a PSF defined as a space-invariant and isotropic Gaussian filter with FWHM= 4.4mm is applied to the output image. A preliminary study conducted on the realistic replicas of [47] shows that the SNR ranges from approximately 10dB on the earlier frames to 20dB on the latter ones. As a consequence, a zero-mean white Gaussian noise with a SNR of 15dB has been added to the synthetic blurred mixtures.

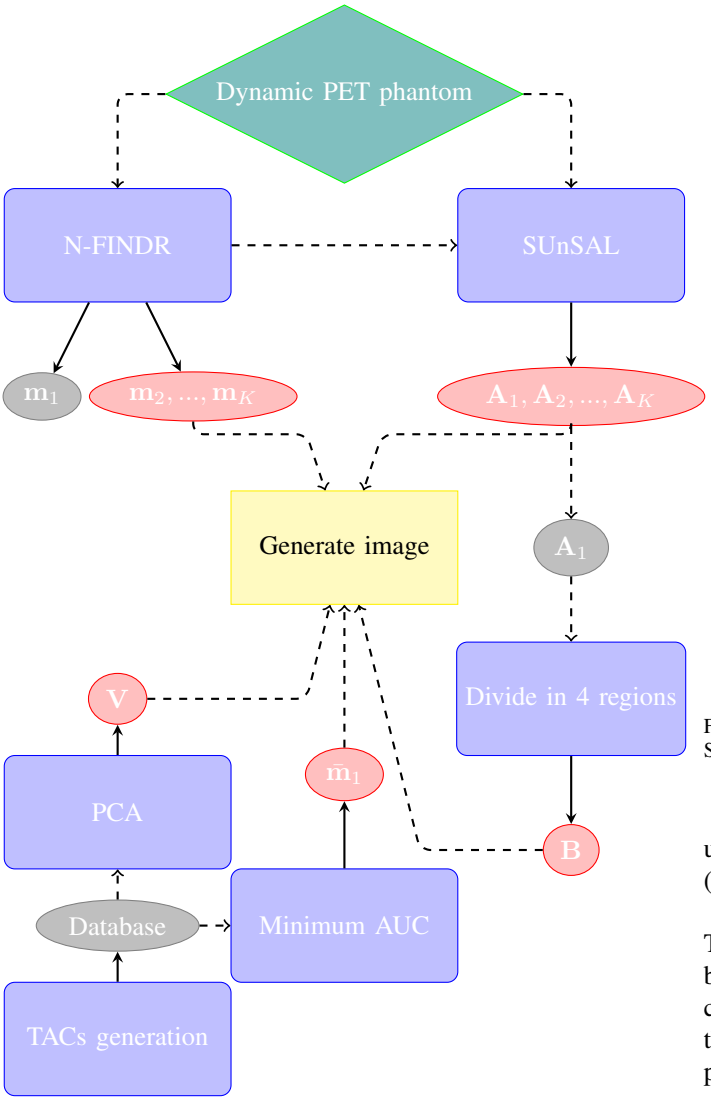

Fig. 3. Model-fitting generation scheme. The red ellipses constitute the ground truth data used for quantitative assessment.

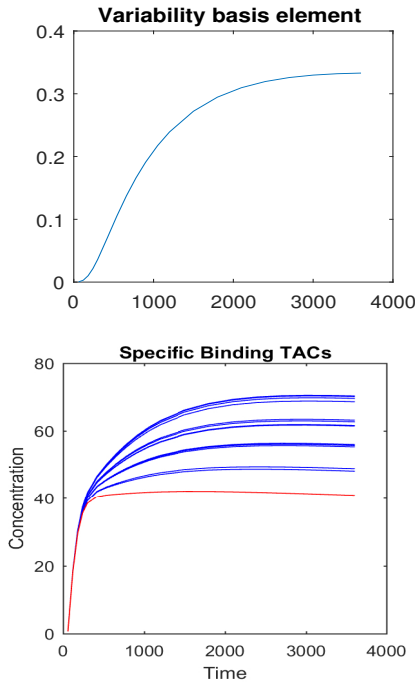

Fig. 4. Top: variability basis element $\mathbf{v}_1$ identified by PCA. Bottom: generated SBE TACs (blue) and the nominal SBE signature (red).

B. Compared methods

The results of the proposed algorithm have been compared to those obtained with several classical linear unmixing methods and other BSS techniques. The methods are recalled below with their most relevant implementation details.

a) FastICA (no variability): ICA is a BSS method that supposes statistical independence between sources and nongaussianity. FastICA measures nongaussianity through an approximation of negentropy to further maximize it with a fixed point iteration scheme [50].

b) NMF (no variability): The NMF algorithm herein applied is based on multiplicative update rules using the Euclidean distance as cost function [51]. The stopping criterion is set to 10^{-3}.

c) VCA/SUnSAL (no variability): The endmember TACs are first extracted using the vertex component analysis (VCA) which requires pure pixels to be present in the analyzed images [52]. The abundances are subsequently estimated by sparse unmixing by variable splitting and augmented Lagrangian (SUnSAL) [49].

d) N-FINDR/SUnSAL (no variability): The endmember TACs are first extracted using N-FINDR [48], a technique based on the fact that the vertices of the largest simplex one can find in a database must be formed by the purest pixels of this database. Per se, it also requires knowledge on the pure pixels. Abundances are also estimated with SUnSAL.

e) LMM-PALM (no variability): To appreciate the interest of explicitly modeling the spatial variability of the SBE TAC, a depreciated version of the proposed PSBE-LMM PALM algorithm is considered. More precisely, LMM PALM uses the LMM (1) without allowing the SBE TAC $\mathbf{m}_{1,n}$ to be spatially varying. The stopping criterion, defined as ε, is set to 10^{-3}. The values of the regularization parameter are reported in Table I.

f) PSBE-LMM PALM: As detailed in Section II-A, matrix $\mathbf{B}$ is constrained to be non-negative to increase accuracy. Consequently, the SBE is initialized as the TAC with the minimum AUC learned from the generated database to ensure a positive $\mathbf{B}$. The regularization parameters have been tuned to the values reported in Table I. As for the other approaches, the stopping criterion is set to 10^{-3}.

All the methods requiring an appropriate endmember TAC initialization have been initialized with the output of a K-means classification. This K-means estimates are also considered for performance comparison. For the proposed method, referred to as PSBE-LMM PALM, the SBE has been initialized with the TAC of minimum AUC from the generated database, i.e., $\bar{\mathbf{m}}_1$.

The performance of the algorithms has been accessed through the use of a normalized mean square error (NMSE)

TABLE I
ABUNDANCE, ENDMEMBER AND VARIABILITY PENALIZATION PARAMETERS FOR LMM PALM AND PSBE-LMM PALM WITH SNR= 15DB

	LMM PALM	PSBE PALM
α	0.010	0.010
β	0.010	0.010
λ	-	0.020
ε	0.001	0.001

computed for each variable

$$\mathrm{NMSE}(\hat{\boldsymbol{\theta}}) = \frac{\|\hat{\boldsymbol{\theta}} - \boldsymbol{\theta}\|_F^2}{\|\boldsymbol{\theta}\|_F^2} \tag{23}$$

where $\hat{\boldsymbol{\theta}}$ is the estimated variable and $\boldsymbol{\theta}$ the corresponding ground truth. The NMSE has been measured separately on the following parameters: the abundance coefficients $\mathbf{A}_1$ corresponding to the SBR, the remaining abundances $\mathbf{A}_{2:K} \triangleq \left[\mathbf{A}_2^T \dots \mathbf{A}_K^T\right]^T$, the SBE TACs in the SBR affected by the variability $\tilde{\mathbf{M}}_1 \triangleq [\mathbf{m}_{1,1}, \dots, \mathbf{m}_{1,N}]$, the endmembers corresponding to the other regions $\mathbf{M}_{2:K} \triangleq [\mathbf{m}_2, \dots, \mathbf{m}_K]$ and finally the variability abundance matrix $\mathbf{B}$.

For a fair comparison taking inherent scale ambiguity into account, results from both ICA and NMF have been normalized with respect to the ground truth for each endmember and abundance class

$$\hat{\mathbf{m}}_k \leftarrow \hat{\mathbf{m}}_k \frac{\|\mathbf{m}_k\|_2}{\|\hat{\mathbf{m}}_k\|_2}, \quad \hat{\mathbf{a}}_k \leftarrow \hat{\mathbf{a}}_k \frac{\|\hat{\mathbf{m}}_k\|_2}{\|\mathbf{m}_k\|_2}. \tag{24}$$

C. Hyperparameter influence

Considering the significant number of hyper-parameters to be tuned in both LMM PALM and PSBE-LMM PALM approaches (i.e., α, β, λ), a full sensitivity analysis is a challenging task, which is further complexified by the non-convex nature of the problem considered. To alleviate this issue, each parameter has been individually adjusted while the others were set to zero. Some simulations conducted with different (non-zero) parameter values but using the same stopping criterion showed that most of the parameter values are only useful to change the number of iterations needed to reach the same convergence point. The parameters have been chosen such that the total percentage of its corresponding term in the overall objective function does not surpass 25% of the total value of the function while its influence can still help the algorithm to converge faster. In terms of abundance, given the high level of noise of those images, the hyperparameter has been set so as to reduce the noise impact while avoiding too much smoothing the abundance maps. The endmember penalization parameter has been chosen through a compromise between the quality of the initial endmember TAC estimates $\mathbf{M}^0$ and the flexibility required by PALM to reach more accurate estimates. Finally the variability penalization has been set to achieve a trade-off between the risks of capturing noise into the variability and of losing information. While there are more automatized ways to choose the hyperparameter values such as cross-validation, grid search, random search and Bayesian estimation, these hyperparameter choices have seemed to be sufficient to assess the performance of the proposed method. The parameter values that has been used for LMM PALM and PSBE-LMM PALM are reported in Table I.

D. Results

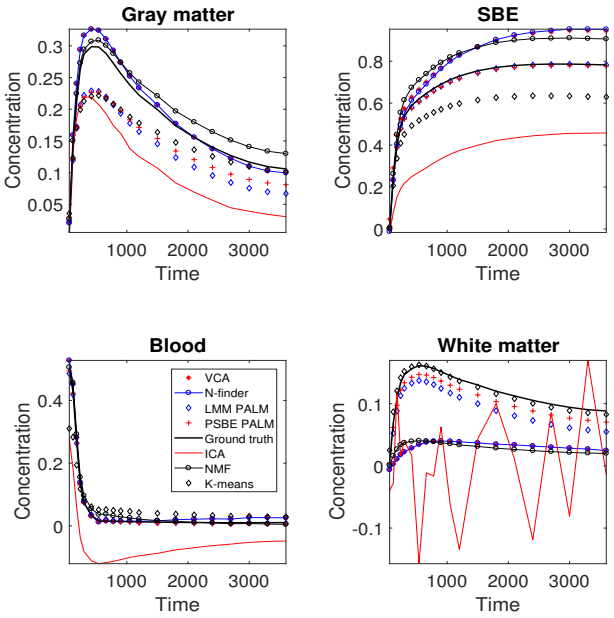

Fig. 5. TACs obtained for SNR=15dB. For the proposed PSBE-LMM PALM algorithm, the represented SBE correspdonds to the empirical mean of the estimated spatially varying SBE TACs $\mathbf{m}_{1,1}, \dots, \mathbf{m}_{1,N}$.

The abundance maps recovered by the compared algorithms are shown in Fig. 6. Each row corresponds to a specific endmember: SBE, white matter endmember, non-specific gray matter endmember, blood endmember (from top to bottom, respectively). The eight columns contain respectively the abundance maps of the ground truth, and the abundances estimated by K-means, ICA, NMF, VCA/SUnSAL, N-FINDR/SUnSAL, LMM PALM and PSBE-LMM PALM (from letft to right, respectively). A visual comparison suggests that the ICA approach gives a reasonable estimation of both the SBE and blood abundance maps, however it failed at estimating correctly the white and non-specific grey matter maps. NMF, VCA/SUnSAL, N-FINDR/SUnSAL provides better estimation results than ICA, with interesting estimations of all four abundance maps. However, the abundance maps obtained with LMM PALM and PSBE-LMM PALM are both closer to the ground truth and more consistent with the expected localization of each endmember in the brain. It can also be observed that the abundance maps obtained with the proposed PSBE-LMM PALM approach present a higher contrast compared to LMM PALM and other approaches. The maps of PSBE-LMM PALM are also sharper compared to LMM PALM.

The corresponding estimated endmember TACs are shown in Fig. 5 where, for comparison purposes, the SBE depicted for PSBE-LMM PALM is the empirical average over the whole set of spatially varying SBE TACs, along with the ground truth TACs. The ICA approach leads to estimations of poor

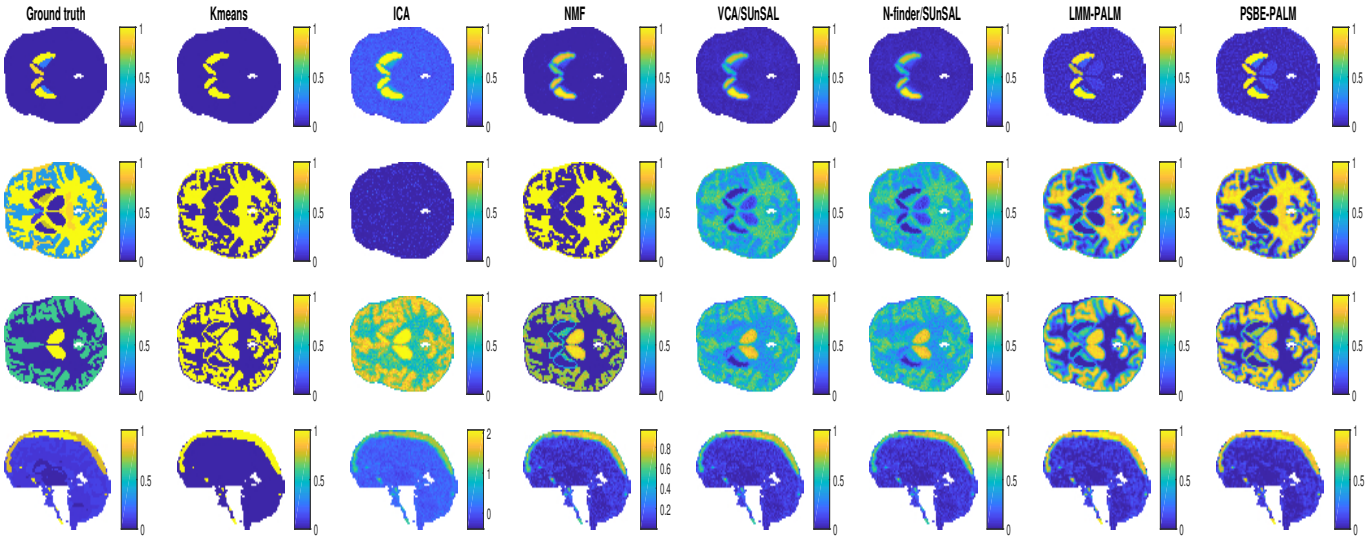

Fig. 6. Abundance maps of the 15th time-frame obtained for SNR=15dB corresponding to the SBR, white matter, gray matter and blood, from top to bottom. The first 3 lines show a transaxial view while the last one shows a sagital view.

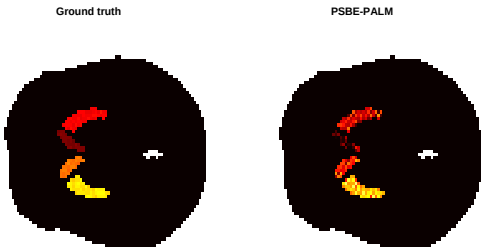

Fig. 7. Ground-truth (left) and estimated (right) SBE variability.

TABLE II
NORMALIZED MEAN SQUARE ERRORS OF ESTIMATED VARIABLES FOR VCA/SUNSAL, N-FINDR/SUNSAL, LMM PALM AND PSBE-LMM PALM WITH SNR=15DB

	$\mathbf{a}_1$	$\mathbf{A}_{2:K}$	$\tilde{\mathbf{M}}^1$	$\mathbf{M}^{2:K}$	$\mathbf{B}$
K-means	0.555	0.649	0.120	0.264	-
ICA	1.445	1.057	0.234	0.810	-
NMF	0.424	2.584	0.495	0.330	-
VCA/SUnSAL	0.518	0.491	0.507	0.332	-
N-FINDR/SUnSAL	0.520	0.497	0.508	0.332	-
LMM PALM	0.469	**0.454**	0.263	0.202	-
PSBE-PALM	**0.378**	0.482	**0.027**	**0.174**	0.273

quality, which is mainly due to the lack of any constraint regarding the endmembers except for their independence. Among the other methods, the best estimation is obtained by the proposed PSBE-LMM PALM approach for the SBE, white matter and blood. The best non specific gray matter endmember estimation has been obtained by VCA/SUnSAL and N-FINDR/SUnSAL, followed by PSBE-LMM PALM and LMM PALM. It can be observed that PSBE-LMM PALM and LMM PALM have slightly underestimated the AUC of this endmember TAC, which has been compensated with higher values in the corresponding variability abundance map. On the contrary, VCA/SUnSAL and N-FINDR/SUnSAL have overestimated the AUC of the SBE, leading to lower abundances for the corresponding maps. PSBE-LMM PALM provides a very precise estimation of the mean SBE.

Table II presents the NMSE for each estimated variable. These quantitative results confirm the preliminary findings drawn from the visual inspection of Fig. 6 and 5. The proposed method outperforms all the others for the estimation of $\tilde{\mathbf{M}}_1$, with a great difference comparing to VCA and N-FINDR. It also shows better results than VCA, N-FINDR and K-means for $\mathbf{A}_{2:K}$ as well and performs better than ICA and NMF, even though it is less effective but still competitive compared to LMM PALM. For all the remaining variables, the proposed method outperforms all the others and validates the importance of considering the SBE TAC variability.

Fig. 5 has shown that the mean of the estimated SBE TACs $\mathbf{m}_{1,1}, \ldots, \mathbf{m}_{1,N}$ is very close to the mean ground truth both for LMM PALM and PSBE-LMM PALM but the computation of the individual error for each voxel shows better performance for PSBE-LMM PALM. It is important to notice the nominal SBE TAC is set from the available database and is not necessarily the minimum AUC TAC present in the SBR of the image. Since the nominal SBE is fixed, as errors on the SBE are only compensated by $\mathbf{B}$ for variations above the initial SBE due to the positive constraint on this parameter, an error on initialization may induce a little bias on $\tilde{\mathbf{M}}_1$.

Due to the high correlation between the endmembers, sparsity penalization has been imposed on the variability coefficients such that this variability remains localized in the SBR. By decreasing the variability error to almost 27%, the quality of the SBR abundance $\mathbf{A}_1$ estimation has been improved. Fig. 7 shows the synthetically generated and estimated variability abundances, whose non zeros values are only localized in 4 subregions with different mean values. Nevertheless, the deconvolution process induces some noise-like artifacts on $\mathbf{B}$, affecting the quality of the

estimation. Meanwhile, the PSF is also responsible for losing possible high-frequency details present in $\mathbf{B}$.

In dynamic PET imaging, the TACs of the different types of tissues are always highly correlated. Consequently, the standard LMM PALM approach converges to poor local optima and is only prevented from finding completely different TACs by the endmember similarity penalization. On the contrary, PSBE-LMM PALM shows better results through adding a sparsity penalization to the specific binding variability while benefiting from the similarity penalization on endmembers. VCA and N-FINDR associated with SUnSAL show acceptable results, considering PET images are highly noisy but PSBE-LMM PALM presents better results in the SBR voxels which is a great advantage since this is an important region.

V. Evaluation on Real Data

A. PET data acquisition

To assess the behavior of the proposed approach on real dynamic PET images, the different methods have been applied to a dynamic PET image with [18F]DPA-714 of a stroke subject. Cerebral stroke is a severe and frequently occurring condition. While different mechanisms are involved in the pathogenesis of stroke, there is an increasing evidence that inflammation, mainly involving the microglial and the immune system cells, account for its pathogenic progression. The [18F]DPA-714 is a ligand of the 18-kDa translocator protein (TSPO) for in vivo imaging, which is a biomarker of neuroinflammation. The subject was examined using an Ingenuity TOF Camera from Philips Medical Systems, seven days after the stroke.

The PET acquisition was reconstructed into a $128 \times 128 \times 90$-voxels dynamic PET image with $L = 31$ time-frames. As for the experiments conducted on simulated data, the voxel TACs are assumed to be mixtures of $K = 4$ types of elementary TAC: specific binding associated with inflammation, blood, the non-specific gray and white matters. The K-means method has been applied to the images to mask the cerebrospinal fluid and further initialize both PALM-based algorithms. The stroke region has been segmented on a registered MRI image to constitute a ground truth of the SBR from which the variability descriptors $\mathbf{V}$ have been learned by PCA. Similarly, the nominal SBE has been fixed as the empirical average of TACs with AUC comprised between the 5th and 10th percentile. The choice to use the average of a percentile instead of the minimum AUC TAC is due to the fact that the database, in this case, is distorted by both the noise and the partial volume effect. Both ICA and NMF results have been normalized with respect to the VCA result since no ground truth is available for real data.

B. Results

Figure 8 depicts the abundance maps obtained for the real image while the corresponding unmixed endmembers are shown in Fig. 9. In the first row, corresponding to SBE, it can be observed that, except ICA, all methods correctly found the main localization of the stroke area. However, we can notice that the proposed PSBE-LMM PALM approach founds a significantly larger area, which is more coherent with the stroke area as found in MRI data. Moreover, for the proposed PSBE-LMM PALM, the abundance map of the SBE shows high values in the thalamus, which is a region known to present specific binding of [18F]DPA-714. Another remarkable results is the abundance maps for the blood. The sagittal view displayed in the last row is in the exact center of the brain. Both NMF and PSBE-LMM PALM found abundance maps that are in very good agreement with the superior sagittal sinus vein that passes on the higher part of the brain. On the contrary, note that both VCA and N-FINDR estimate two endmembers which are mixtures of the vein TACs and other regions. Meanwhile, the two PALM-based algorithms find four different regions, where SBE seems to be more precise. To have a better look at the variability and SBE abundance, Fig. 10 shows the comparison of the initialization with the PSBE-PALM resultant SBR abundance, the estimated SBR variability and the expected SBR extracted from a MRI image. It is possible to see an interesting improvement in comparison to the initialization, showing that the method converges to an accurate and relevant estimation of the SBR.

VI. Conclusion and Future Works

This paper introduced a new paradigm to conduct kinetic component analysis of dynamic PET images. It relied on the unmixing concept accounting for specific binding TACs variation. The method was based on the hypothesis that variations within the SBR can be described by a small number of basis elements and their corresponding proportions per voxel. The resulting optimization problem is extremely non-convex with highly correlated endmembers and variability basis elements, which leads to a high number of spurious local optima for the cost function. The performance of the method on synthetic data showed its strong potential impact for dynamic PET image analysis. Indeed, the proposed approach compared favorably with state-of-the-art unmixing approaches while providing the ability to focus on a better estimation of specific binding variable. The proposed approach has many potential applications in dynamic PET imaging. It could be used for the segmentation of ROI, classification of the voxels, creation of subject-specific kinetic reference regions or even simultaneous filtering and partial volume correction. Besides exploring such applications of the method, future works should focus on the introduction of a Poisson-fitting measure of divergence used in the cost function, e.g. Kullback-Leibler, to better model noise frequently encountered in low rate PET data.

References

[1] M. E. Kamasak, "Clustering dynamic PET images on the Gaussian distributed sinogram domain," *Comput. Methods Programs Biomed.*, vol. 93, pp. 217–227, 2009.

[2] K.-P. Wong, D. Feng, S. R. Meikle, and M. J. Fulham, "Segmentation of dynamic PET images using cluster analysis," *IEEE Trans. Nuclear Sci.*, vol. 49, no. 1, February 2002.

[3] J. Ashburner, J. Haslam, C. Taylor, V. J. Cunningham, and T. Jones, *A Cluster Analysis Approach for the Characterization of Dynamic PET Data*. Academic Press, 1996, ch. 59, pp. 301–306.

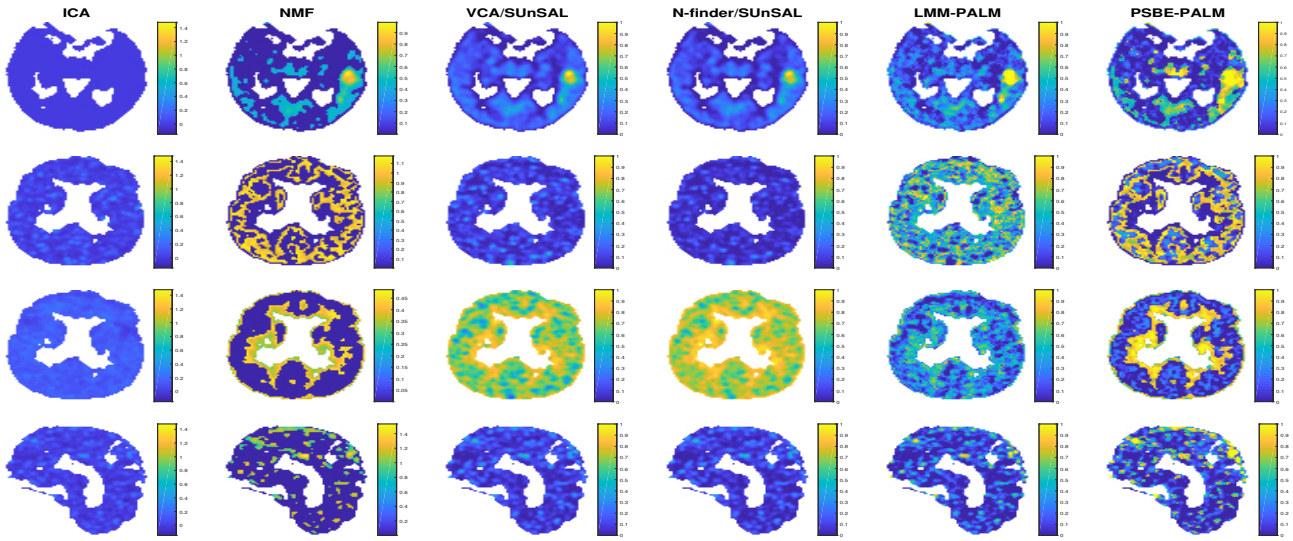

Fig. 8. Abundance maps of the real image, where the first 4 lines show a transaxial view while the last one shows a sagital view. From top to botto, the SBR, white matter, gray matter and blood.

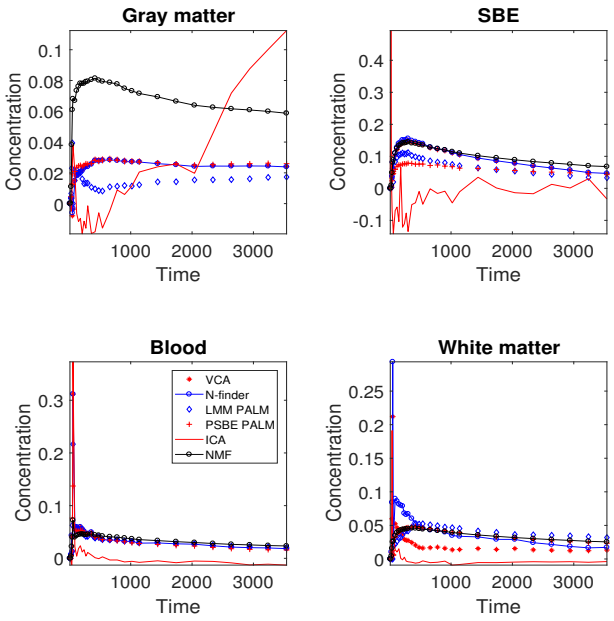

Fig. 9. TACs obtained by estimation from the real image.

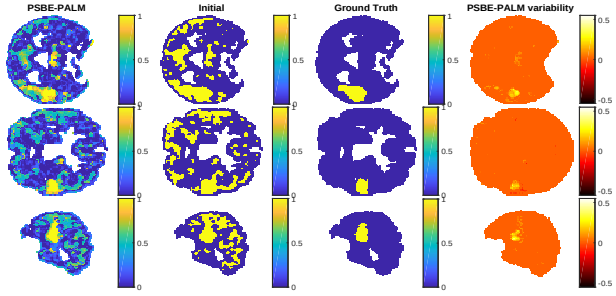

Fig. 10. View of the 3 dimensions of SBR. From left to right: PSBE-LMM PALM result, k-means initialization result, MRI ground-truth and estimated variability matrix

[4] J. Brankov, N. Galatsanos, Y. Yang, and M. Wernick, "Segmentation of dynamic PET or fMRI images based on a similarity metric," *IEEE Trans. Nuclear Sci.*, vol. 50, no. 5, pp. 1410–1414, Oct 2003.

[5] Y. Zhou, S.-C. Huang, M. Bergsneider, and D. F. Wong, "Improved parametric image generation using spatial-temporal analysis of dynamic PET studies," in *NeuroImage*, Elsevier, Ed., vol. 15, 2002, pp. 697–707.

[6] H. Guo, R. Renaut, K. Chen, and E. Reiman, "Clustering huge data sets for parametric PET imaging," *Biosystems*, vol. 71, no. 1-2, pp. 81–92, Sep 2003.

[7] R. Maroy, R. Boisgard, C. Comtat, V. Frouin, P. Cathier, E. Duchesnay, F. Dolle, P. Nielsen, R. Trebossen, and B. Tavitian, "Segmentation of rodent whole-body dynamic PET images: An unsupervised method based on voxel dynamics," *IEEE Trans. Med. Imag.*, vol. 27, no. 3, pp. 342–354, Mar 2008.

[8] J. Cheng-Liao and J. Qi, "Segmentation of mouse dynamic PET images using a multiphase level set method," *Physics Med. Biol.*, vol. 55, pp. 6549–6569, 2010.

[9] S. Mouysset, H. Zbib, S. Stute, J. M. Girault, J. Charara, J. Noailles, S. Chalon, I. Buvat, and C. Tauber, "Segmentation of dynamic PET and images with kinetic spectral clustering," *Physics Med. Biol.*, vol. 58, pp. 6931–6944, 2013.

[10] R. B. Innis, V. J. Cunningham, J. Delforge, M. Fujita, A. Gjedde, R. N. Gunn, J. Holden, S. Houle, S.-C. Huang, M. Ichise, and et al., "Consensus nomenclature for in vivo imaging of reversibly binding radioligands," *J. Cereb. Blood Flow Metab*, vol. 27, no. 9, pp. 1533–1539, May 2007.

[11] H.-M. Wu, C. K. Hoh, Y. Choi, H. R. Schelbert, R. A. Hawkins, M. E. Phelps, and S.-C. Huang, "Factor analysis for extraction of blood time-activity curves in dynamic FDG-PET studies," *J. Nuclear Med.*, vol. 36, no. 9, pp. 1714–1722, September 1995.

[12] M. Margadan-Mendez, A. Juslin, S. V. Nesterov, K. Kalliokoski, J. Knuuti, and U. Ruotsalainen, "ICA based automatic segmentation of dynamic $H_2{}^{15}o$ cardiac PET images," *IEEE Trans. Info. Technology Biomed.*, vol. 14, no. 3, pp. 795–802, May 2010.

[13] J. S. Lee, D. S. Lee, J. Y. Ahn, G. J. Cheon, S.-K. Kim, J. S. Yeo, K. Seo, K. S. Park, J.-K. Chung, and M. C. Lee, "Blind separation of cardiac components and extraction of input function from $H^{15}{}_2O$ dynamic myocardial PET using independent and component analysis," *J. Nuclear Med.*, vol. 42, no. 6, pp. 938–943, 2001.

[14] K. Chen, X. Chen, R. Renaut, G. E. Alexander, D. Bandy, H. Guo, and E. M. Reiman, "Characterization of the image-derived carotid artery input function using independent component analysis for the quantitation of [18F] fluorodeoxyglucose positron emission tomography images," *Physics Med. Biol.*, vol. 52, pp. 7055–7071, 2007.

[15] J. Nascimento and J. Dias, "Does independent component analysis play a role in unmixing hyperspectral data?" *IEEE Trans. Geosci. Remote Sens.*, vol. 43, no. 1, pp. 175–187, Jan 2005.

[16] J. S. Lee, D. D. Lee, S. Choi, K. S. Park, and D. S. Lee, "Non-negative

matrix factorization of dynamic images in nuclear medicine," in *Proc. IEEE Nuclear Sci. Symp (NSS)*, 2001.

[17] K. M. Kim, H. Watabe, M. Shidahara, J. Y. Ahn, S. Choi, N. Kudomi, K. Hayashida, Y. Miyake, and H. Iida, "Noninvasive estimation of cerebral blood flow using image-derived carotid input function in $H_2{}^{15}O$ dynamic PET," in *Proc. IEEE Nuclear Sci. Symp (NSS)*, 2001, pp. 1282–1285.

[18] B. Bodvarsson, L. K. H. C. Svarer, and G. Knudsen, "NMF on positron emission tomography," in *Proc. IEEE Int. Conf. Acoust., Speech and Signal Process. (ICASSP)*, vol. I, 2007, pp. 309–312.

[19] D. Schulz, "Non-negative matrix factorization based input function extraction for mouse imaging in small animal PET - comparison with arterial blood sampling and factor analysis," *J. Molecular Imag. Dynamics*, vol. 02, 2013.

[20] W. S. B. Ouedraogo, A. Souloumiac, M. Jaidane, and C. Jutten, "Non-negative blind source separation algorithm based on minimum aperture simplicial cone," *IEEE Trans. Signal Process.*, vol. 62, no. 2, pp. 376–389, Jan 2014.

[21] R. Boutchko, D. Mitra, S. L. Baker, W. J. Jagust, and G. T. Gullberg, "Clustering-initiated factor analysis application for tissue classification in dynamic brain positron emission tomography." *J. Cereb. Blood Flow Metab.*, vol. 35, no. 7, pp. 1104–11, jul 2015.

[22] J.-W. Lin, A. F. Laine, and S. R. Bergmann, "Improving PET-based physiological quantification through methods of wavelet denoising," *IEEE Trans. Biomed. Eng.*, vol. 48, no. 2, pp. 202–212, 2001.

[23] J. M. Links, J. P. Leal, H. W. Mueller-Gaertner, and H. N. Wagner, "Improved positron emission tomography quantification by Fourier-based restoration filtering," *Eur. J. Nuclear Med.*, 1992.

[24] B. T. Christian, N. T. Vandehey, J. M. Floberg, and C. A. Mistretta, "Dynamic PET denoising with HYPR processing," *J. Nuclear Med.*, vol. 51, no. 7, pp. 1147–1154, Jun 2010.

[25] F. Turkheimer, J. Aston, R. Banati, C. Riddell, and V. Cunningham, "A linear wavelet filter for parametric imaging with dynamic PET," *IEEE Trans. Med. Imag.*, vol. 22, no. 3, pp. 289–301, Mar 2003.

[26] P. Millet, V. Ibanez, J. Delforge, S. Pappata, and J. Guimon, "Wavelet analysis of dynamic PET data: Application to the parametric imaging of benzodiazepine receptor concentration," *NeuroImage*, vol. 11, no. 5, pp. 458–472, May 2000.

[27] C. Tauber, S. Stute, M. Chau, P. Spiteri, S. Chalo, D. Guilloteau, and I. Buvat, "Spatio-temporal diffusion of dynamic PET images," *Physics Med. Biol.*, vol. 56, pp. 6583–6596, 2011.

[28] R. N. Gunn, A. A. Lammertsma, S. P. Hume, and V. J. Cunningham, "Parametric imaging of ligand-receptor binding in PET using a simplified reference region model," *NeuroImage*, vol. 6, pp. 279–287, 1997.

[29] C. Schiepers, W. Chen, M. Dahlbom, T. Cloughesy, C. K. Hoh, and S.-C. Huang, "18F-fluorothymidine kinetics of malignant brain tumors," *Eur. J. Nuclear Med. Molecular Imag.*, vol. 34, no. 7, pp. 1003–1011, Feb 2007.

[30] M. E. Kamasak, "Computation of variance in compartment model parameter estimates from dynamic PET data," in *Proc. IEEE Int. Symp. Biomed. Imag. (ISBI)*, 2012.

[31] P. Razifar, M. Sandstrom, H. Schnieder, B. Langstrom, E. Maripuu, E. Bengtsson, and M. Bergstrom, "Noise correlation in PET, CT, SPECT and PET/CT data evaluated using autocorrelation function: a phantom study on data, reconstructed using FBP and OSEM," *BMC Med. Imag.*, vol. 5, no. 1, Aug 2005.

[32] R. Boellaard, A. van Lingen, and A. A. Lammertsma, "Experimental and clinical evaluation of iterative reconstruction (OSEM) in dynamic PET: Quantitative characteristics and effects on kinetic modeling," *J. Nuclear Med.*, vol. 42, no. 5, pp. 808–817, 2001.

[33] J. M. Bioucas-Dias, A. Plaza, N. Dobigeon, M. Parente, Q. Du, P. Gader, and J. Chanussot, "Hyperspectral unmixing overview: Geometrical, statistical, and sparse regression-based approaches," *IEEE J. Sel. Topics Appl. Earth Observations Remote Sens.*, vol. 5, no. 2, pp. 354–379, Apr 2012.

[34] Y. Huang, A. K. Zaas, A. Rao, N. Dobigeon, PETer J. Woolf, T. Veldman, N. C. Oien, M. T. McClain, J. B. Varkey, B. Nicholson, L. Carin, S. Kingsmore, C. W. Woods, G. S. Ginsburg, and A. Hero, "Temporal dynamics of host molecular responses differentiate symptomatic and asymptomatic influenza A infection," *PLoS Genetics*, vol. 8, no. 7, Aug. 2011.

[35] N. Dobigeon and N. Brun, "Spectral mixture analysis of EELS spectrum-images," *Ultramicroscopy*, vol. 120, pp. 25–34, Sept. 2012.

[36] S. Moussaoui, D. Brie, and J. Idier, "Non-negative source separation: range of admissible solutions and conditions for the uniqueness of the solution," in *Proc. IEEE Int. Conf. Acoust., Speech and Signal Process. (ICASSP)*, 2005.

[37] D. Donoho and V. Stodden, "When does non-negative matrix factorization give a correct decomposition into parts?" in *Advances in Neural Information Processing Systems 16*. Adv. in Neural Information Process. Systems, 2004.

[38] A. Zare and K. Ho, "Endmember variability in hyperspectral analysis: Addressing spectral variability during spectral unmixing," *IEEE Signal Process. Mag.*, vol. 31, no. 1, pp. 95–104, Jan 2014.

[39] A. Halimi, N. Dobigeon, and J.-Y. Tourneret, "Unsupervised unmixing of hyperspectral images accounting for endmember variability," *IEEE Trans. Image Process.*, vol. 24, no. 12, pp. 4904–4917, Dec 2015.

[40] P.-A. Thouvenin, N. Dobigeon, and J.-Y. Tourneret, "Hyperspectral unmixing with spectral variability using a perturbed linear mixing model," *IEEE Trans. Signal Process.*, vol. 64, no. 2, pp. 525–538, 2016.

[41] S.-U. Park, N. Dobigeon, and A. O. Hero, "Variational semi-blind sparse deconvolution with orthogonal kernel bases and its application to MRFM," *Signal Process.*, vol. 94, pp. 386–400, Jan. 2014.

[42] S. Pajevic, M. E. Daube-Witherspoon, S. L. Bacharach, and R. E. Carson, "Noise characteristics and of 3d and 2d PET and images," in *IEEE Trans. Med. Imag.*, vol. 17, no. 1, Feb. 1998, pp. 1–23.

[43] J. Dutta, R. M. Leahy, and Q. Li, "Non-local means denoising of dynamic PET images," *PLoS ONE*, vol. 8, no. 12, p. e81390, Dec 2013.

[44] R. Tibshrani, "Regression shrinkage and selection via the lasso," *J. Roy. Stat. Soc.*, vol. 58, no. 1, pp. 267–288, 1996.

[45] J. Bolte, S. Sabach, and M. Teboulle, "Proximal alternating linearized minimization for nonconvex and nonsmooth problems," *Math. Programming*, vol. 146, no. 1-2, pp. 459–494, Jul 2013.

[46] L. Condat, "Fast projection onto the simplex and the l_1-ball," *Math. Programming*, vol. 158, no. 1-2, pp. 575–585, Sep 2015.

[47] S. Stute, C. Tauber, C. Leroy, M. Bottlaender, V. Brulon, and C. Comtat, "Analytical simulations of dynamic PET scans with realistic count rates properties," in *Proc. IEEE Nuclear Sci. Symp. Med. Imag. Conf. (NSS-MIC)*, Nov. 2015.

[48] M. E. Winter, "N-findr: an algorithm for fast autonomous spectral end-member determination in hyperspectral data," in *Proc. SPIE Imaging Spectrometry V*, M. R. Descour and S. S. Shen, Eds., vol. 3753, no. 1. SPIE, 1999, pp. 266–275.

[49] J. M. Bioucas-Dias and M. A. T. Figueiredo, "Alternating direction algorithms for constrained sparse regression: Application to hyperspectral unmixing," in *Proc. IEEE GRSS Workshop Hyperspectral Image SIgnal Process.: Evolution in Remote Sens. (WHISPERS)*, 2010.

[50] A. Hyvärinen and E. Oja, "Independent component analysis: Algorithms and applications," *Neural Networks*, pp. 411–430, 2000.

[51] D. D. Lee and H. S. Seung, "Algorithms for non-negative matrix factorization," in *Proc. Neural Info. Process. Syst. (NIPS)*, 2000.

[52] J. Nascimento and J. Dias, "Vertex component analysis: a fast algorithm to unmix hyperspectral data," *IEEE Trans. Geosci. Remote Sens.*, vol. 43, no. 4, pp. 898–910, Apr 2005.